European Journal of Mechanics / B Fluids 108 (2024) 211–225

Contents lists available at ScienceDirect

European Journal of Mechanics / B Fluids

journal homepage: www.elsevier.com/locate/ejmflu

Numerical simulation of deep-water wave breaking using RANS: Comparison with experiments

Yuxuan Liu [a,*], Ton S. van den Bremer [b], Thomas A.A. Adcock [a]

[a] Department of Engineering Science, University of Oxford, Oxford, OX1 3PJ, United Kingdom
[b] Faculty of Civil Engineering and Geosciences, Delft University of Technology, Delft, 2628 CD, The Netherlands

ARTICLE INFO

Keywords:
Wave breaking
Nonlinear processes
Computational Fluid Dynamics
Reynolds-averaged turbulence model

ABSTRACT

Wave breaking is a multifaceted physical phenomenon that is not fully understood and remains challenging to model. An effective method for investigating wave breaking involves utilising the two-phase Reynolds-averaged Navier–Stokes (RANS) equations to directly simulate breaking waves. In this study, we apply a RANS model with an adaptively refined mesh to simulate breaking waves in deep water using the stabilised RANS model proposed by Larsen and Fuhrman. This approach enables a more efficient simulation of the physics of breaking waves compared to Direct Numerical Simulations, as it places less stringent demands on grid resolution. Our findings demonstrate that the RANS model compares well with deep water wave breaking experiments in terms of surface elevation. We also give estimates of the breaking strength parameter of our RANS simulations and compared them with the literature.

1. Introduction

Wave breaking is an important phenomenon in the ocean, yet many aspects of it remain poorly understood. Wave breaking dominates energy dissipation in the ocean [1]. Energy dissipation related to breaking involves a complex combination of energy transfer and energy dissipation mechanisms. In order to understand these mechanisms, many Computational Fluid Dynamics (CFD) methods including Direct Numerical Simulation (DNS), Large-Eddy Simulation (LES), and Reynolds-Averaged simulation (RANS) have been used to solve the two-phase Navier–Stokes equations. Although DNS and LES simulations have become feasible given increasing computing resources, it is still very expensive to perform parametric studies with these methods. Full-scale DNS simulation is difficult and resource-demanding even for systems at laboratory scale. Hence, the focus of this paper is on RANS simulation as a relatively cheap way to study wave breaking that can ultimately be used to generate a large ensemble of simulations, suitable, for example, for machine-learning applications.

A well-known issue affecting RANS simulations is that all standard turbulence models, such as $\kappa-\epsilon$ or $\kappa-\omega$, overestimate the generation of turbulent kinetic energy (TKE) in the near-potential flow region. The overproduction of TKE can cause an underestimated wave height at the onset of the breaking or during the breaking. This underestimation has been reported in existing studies [2–4]. Many numerical studies of breaking waves adopt the non-stabilised $\kappa-\epsilon$ or $\kappa-\omega$ model [5–8]. However, in recent years, this issue has been successfully addressed by switching to a modified $\kappa-\omega$ model or to a Reynolds Stress Equation Model (RSM) [9,10]. Specifically, the unbounded growth of TKE leads to unphysical damping of surface waves. This issue appears due to an incorrect prediction of the generation of turbulence from the potential-flow motion. The conditional stability of $\kappa-\omega$ models was shown by Mayer and Madsen [11]. Wilcox [12] proposed a revised $\kappa-\omega$ model with a stress limiter to improve the prediction of TKE in anisotropic regions such as shock wave boundary layers and stagnation points. Following their work, Larsen and Fuhrman [9] investigated the stability of several RANS models including the revised models [11,12] under (potential-flow) gravity-wave perturbations, leading to the proposal of a new ω-limiter to stabilise the $\kappa-\omega$ model of Wilcox [12,13].

Several studies of breaking waves [14–17] have been performed with the revised turbulence model of Larsen and Fuhrman [9] and report close agreement between experiments and simulations for shallow-water breaking waves. In very recent work, simulations with Wilcox's stress-ω model [18] have been performed for modulated plane waves in deep water. These simulations compare well with experimental

* Corresponding author.
E-mail address: yuxuan.liu@eng.ox.ac.uk (Y. Liu).

https://doi.org/10.1016/j.euromechflu.2024.08.003
Received 4 April 2024; Received in revised form 9 August 2024; Accepted 12 August 2024
Available online 14 August 2024

measurements in terms of spectral downshifting. To our knowledge, deep water wave breaking has not been successfully studied.

The goal of this paper is to introduce an implementation of the RANS model for the purpose of near-energy-conserving (in the absence of breaking) simulation of breaking surface gravity waves on deep water with Adaptive Mesh Refinement (AMR) to enable relatively cheap computation of large ensembles of 2D simulations of breaking waves. We show that the stabilised $\kappa-\omega$ model proposed by Larsen and Fuhrman [9] works well with AMR, and the result agrees satisfactorily with experimental measurements by Eeltink et al. [19]. Estimates of the breaking parameter [20] obtained from our RANS simulations are in reasonable agreement with the parametrisation by Romero et al. [21]. Moreover, we show that the total energy loss outside of the breaking phase is less than 2% in most cases and that viscous dissipation has a negligible contribution.

This paper will be organised as follows. In Section 2 we introduce the numerical model that we use to perform the RANS simulations. In Section 3 we discuss the convergence of the simulation for Stokes waves and a focused wave group case. In Section 4 we will analyse the results we obtained from the model and compare to experimental measurements from Eeltink et al. [19] for three different types of waves (modulated plane waves, focussed wave groups and random waves). We conclude and discuss the validity of the model in Section 5.

2. Methodology

2.1. Navier–Stokes equations

We use the open-source numerical package 'Basilisk' [22] to solve two-phase Reynolds-Averaged Navier–Stokes (RANS) equations on a 2D grid that uses AMR. Momentum conservation is achieved by applying the momentum-conserving volume-of-fluid (VOF) scheme. Mass, momentum and volume conservation are described by:

$$\frac{\partial \rho}{\partial t}+\frac{\partial(\rho u_i)}{\partial x_j}=0, \tag{1}$$

$$\frac{\partial(\rho u_i)}{\partial t}+\frac{\partial(\rho u_j u_i)}{\partial x_j}=-\frac{\partial p}{\partial x_i}+\frac{\partial \sigma_{ij}}{\partial x_i}+\frac{\partial \tau_{ij}}{\partial x_j}+\rho g_i, \tag{2}$$

$$\frac{\partial u_i}{\partial x_i}=0, \tag{3}$$

where u is the mean velocity field, ρ is the fluid density, p is the pressure, g is gravity force vector, σ is the viscous stress tensor in incompressible flow that is defined as $\sigma_{ij}=2\mu S_{ij}$, μ is the fluid dynamic viscosity, $S_{ij}=(\partial u_j/\partial x_i+\partial u_i/\partial x_j)/2$ (as defined in Eq. (7)), τ_{ij} is the Reynolds stress tensor. In this study, the effect of surface tension is ignored. The density ρ and the viscosity μ change according to the volume fraction field $c(\mathbf{x},t)$, where c is bounded within the range $[0,1]$.

2.2. The $\kappa-\omega$ turbulence model

This subsection sets out the equations for the turbulence model we consider in this paper. More details and theoretical background can be found in Wilcox [12]. We implement a RANS turbulence model to approximate the Reynolds stress tensor τ_{ij} in Eq. (2) based on the $\kappa-\omega$ Two-Equation Model [12]. Using the Boussinesq approximation [23] for incompressible flow, we define $\tau_{ij}=2\rho\nu_t\left[S_{ij}-1/3\left(\partial u_k/\partial x_k\right)\delta_{ij}\right]-2/3\rho\kappa\delta_{ij}$, where ν_t is the turbulent eddy viscosity and κ is the turbulence kinetic energy. The $-1/3\partial u_k/\partial x_k$ term vanishes in incompressible flow. In practice, the turbulent normal stress ($2/3\rho\kappa\delta_{ij}$ term) can be either absorbed by the pressure term in the momentum Eq. (2), or neglected in linear two-equation turbulence models. Following practical notes of Rumsey [24], we choose to neglect the turbulent normal stress in the momentum equation. Therefore, only the deviatoric anisotropic stress components are involved in the simulation.

It has been shown by Larsen and Fuhrman [9] that the 'standard' version of the $\kappa-\omega$ model [12] is unstable to perturbations in the near-potential-flow region. The turbulence kinetic energy (TKE) is subject to unbounded growth under the influence of a Stokes wave. Hence, we adopt a modified version of this model with a specific stress limiter that has been introduced to solve this problem [9]. The conservative form of the $\kappa-\omega$ model in incompressible flow with buoyancy correction is written as follows [9], given that κ is the modelled TKE and ω is the modelled turbulence dissipation rate:

$$\frac{\partial(\rho\kappa)}{\partial t}+\frac{\partial(\rho u_j\kappa)}{\partial x_j}=P-\rho\alpha_b^* N^2-\beta^*\rho\omega\kappa+\frac{\partial}{\partial x_j}\left[\left(\mu+\sigma_\kappa\frac{\rho\kappa}{\omega}\right)\frac{\partial\kappa}{\partial x_j}\right], \tag{4}$$

$$\frac{\partial(\rho\omega)}{\partial t}+\frac{\partial(\rho u_j\omega)}{\partial x_j}=\frac{\bar\gamma\omega}{\kappa}P-\beta\rho\omega^2+\frac{\partial}{\partial x_j}\left[\left(\mu+\sigma_\omega\frac{\rho\kappa}{\omega}\right)\frac{\partial\omega}{\partial x_j}\right]+\frac{\rho\sigma_d}{\omega}\frac{\partial\kappa}{\partial x_j}\frac{\partial\omega}{\partial x_j}, \tag{5}$$

where

$$P=\tau_{ij}\frac{\partial u_i}{\partial x_j}, \tag{6}$$

$$S_{ij}=\frac{1}{2}\left(\frac{\partial u_i}{\partial x_j}+\frac{\partial u_j}{\partial x_i}\right), \tag{7}$$

$$\mu_t=\frac{\rho\kappa}{\tilde\omega}, \tag{8}$$

$$\tilde{\tilde\omega}=\max\left[\tilde\omega,\quad\lambda_1\sqrt{\frac{2S_{ij}S_{ij}-\alpha_b^* N^2}{\beta^*}}\right], \tag{9}$$

$$\tilde\omega=\max\left[\tilde{\tilde\omega},\quad\lambda_2\frac{\beta}{\beta^*\bar\gamma}\frac{S_{ij}S_{ij}}{\Omega_{ij}\Omega_{ij}}\omega\right], \tag{10}$$

$$N^2=\frac{g_i}{\rho}\frac{\partial\rho}{\partial x_i}, \tag{11}$$

and the constants and other parameters are:

$$\sigma_\kappa=0.6,\quad\sigma_\omega=0.5,\quad\beta^*=0.09, \tag{12}$$

$$\bar\gamma=\frac{13}{25},\quad\beta_0=0.0708,\quad\beta=\beta_0 f_\beta, \tag{13}$$

$$\lambda_1=0.875,\quad\lambda_2=0.05,\quad\alpha_b^*=1.36, \tag{14}$$

$$f_\beta=\frac{1+85\chi_\omega}{1+100\chi_\omega},\quad\chi_\omega=\left|\frac{\Omega_{ij}\Omega_{jl}\hat S_{li}}{(\beta^*\omega)^3}\right|, \tag{15}$$

$$\hat S_{li}=S_{li}-\frac{1}{2}\frac{\partial u_m}{\partial x_m}\delta_{li},\quad\Omega_{ij}=\frac{1}{2}\left(\frac{\partial u_i}{\partial x_j}-\frac{\partial u_j}{\partial x_i}\right), \tag{16}$$

$$\sigma_d=\begin{cases}0 & \text{for}\quad\dfrac{\partial\kappa}{\partial x_j}\dfrac{\partial\omega}{\partial x_j}\le 0,\\ 0.125 & \text{for}\quad\dfrac{\partial\kappa}{\partial x_j}\dfrac{\partial\omega}{\partial x_j}>0.\end{cases} \tag{17}$$

For the 2D problem we examine, we turn off the 'Pope Correction' [25,26] and set $\chi_\omega=0$.

2.3. Adaptive mesh refinement

We solve the above mentioned Navier–Stokes equations in conjunction with the RANS model with an adaptively refined mesh. An adaptively refined mesh refines or coarsens elements in different regions according to specific criteria, such as the error estimates of the solution or the presence of steep gradients. Basilisk adopted a quadtree data structure to efficiently traverse the 2D mesh at different resolution levels. A quadtree is a tree data structure in which each node has exactly four children. In the context of 2D adaptive mesh refinement, a quadtree divides a 2D domain into four quadrants recursively. Each node in the quadtree represents a square region of the domain, and each division into four children corresponds to a refinement of that region. Further details of the mesh refinement scheme used are given in Popinet [22].

An error estimator assesses the local error in the solution across the mesh. Based on the error estimates, the quadtree structure is refined

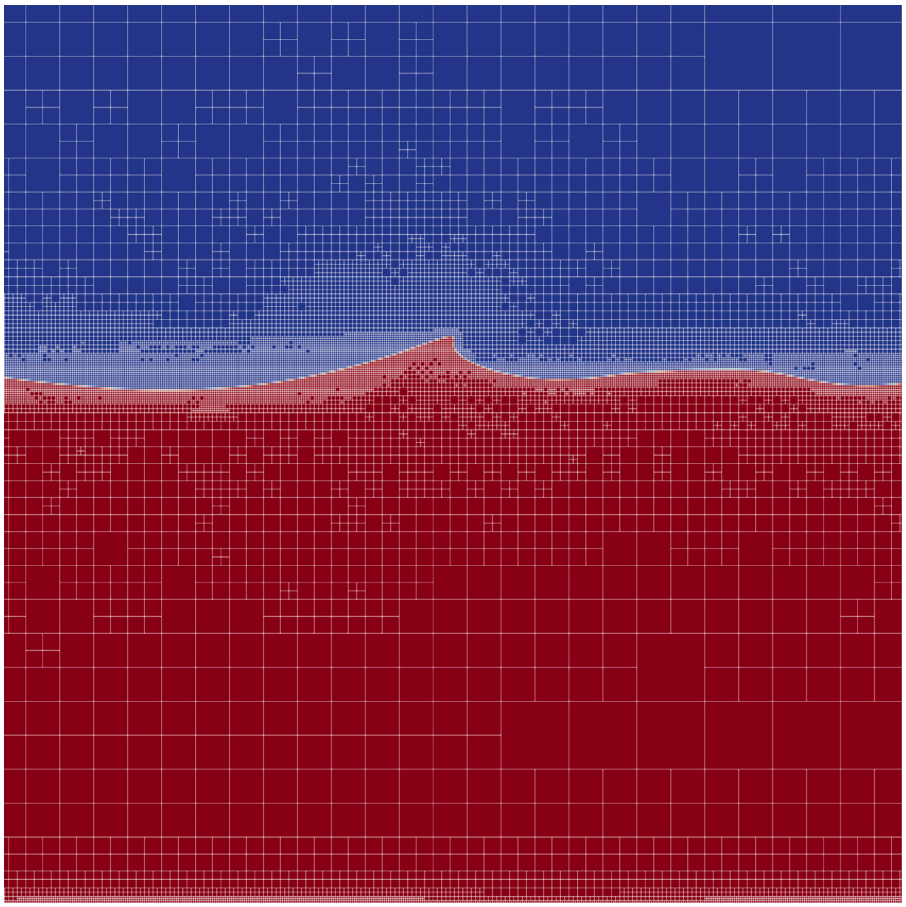

Fig. 1. A snapshot of the mesh during breaking. The mesh is refined adaptively based on the local error of velocity and volume fraction. The interface and the bottom boundary is enforced to maximum resolution at all time. The maximum resolution of this simulation is $0.0032\lambda_0$, where λ_0 is the carrier wave length.

by subdividing nodes into regions with high error and potentially coarsened by merging nodes in regions with low error. This results in a new, adaptively refined mesh. The process iterates, solving the partial differential equations on the refined mesh, reestimating the error, and further refining the mesh until the solution meets the desired accuracy criteria. In this study, we evaluated the local error of the velocity and volume fraction. In addition, we enforce the grid resolution near the air–water interface and the bottom boundary to the maximum (Fig. 1). We also performed a validation study to help determine the appropriate maximum grid resolution.

Prolongation and restriction of field variables are required when coarsening and refining the mesh. Prolongation transfers information from a coarse mesh to a fine mesh, and restriction is its complementary process. They must be processed with care to ensure that the adapted solution still satisfies the conservation of mass and momentum. We adopt default settings of Basilisk for velocity and volume fraction field [22]. For the turbulence variables κ and ω, we use the bilinear interpolation method for prolongation and the volume average method for restriction.

2.4. Wave parameters

We perform simulations for three types of wave conditions:

1. Modulated plane waves;
2. Focused wave groups;
3. Random waves.

We compare our numerical simulation with the experiments of Eeltink et al. [19]. We choose 4 modulated plane wave cases, 2 focused wave group cases, and 4 random wave cases to investigate. Then, we study 300 random simulations generated by the same sets of parameter ranges for these three wave types used in laboratory experiments in Eeltink et al. [19], and a brief summary is given as follows.

2.4.1. Modulated plane waves

We initialise our modulated plane wave case following Eeltink et al. [19] as

$$\eta(x,0) = a_0\left[\sqrt{b_c}\sin(k_0 x) + \sqrt{b_+}\sin(k_+ x + \psi) + \sqrt{b_-}\sin(k_- x + \psi)\right], \quad (18)$$

where the upper and lower sideband frequencies are set according to $\omega_\pm = \omega_0 \pm \Delta\omega$ with $\Delta\omega$ the modulational frequency, and ψ is the phase shift of the sidebands compared to the carrier wave. The sideband wavenumbers $k_\pm$ are calculated using the linear dispersion relationship $\omega_\pm^2 = gk_\pm \tanh(k_\pm d)$. The amplitudes of the carrier wave and the upper and lower sidebands are set according to $a_c = a_0\sqrt{b_c}$, $a_+ = a_0\sqrt{b_+}$ and $a_- = a_0\sqrt{b_-}$, where $b_c = 1 - b_F$, $b_+ = (1 - b_c)/2$, and $b_- = (1 - b_c)/2$, respectively, and b_F is the sideband fraction. The water depth $d = 0.8$ m. In Table 1 we list the specific cases we investigate in Section 4.1.

2.4.2. Focused wave groups and random waves

Focused wave groups and random waves were generated from the JONSWAP [27] spectral density $S(\omega)$:

$$S(\omega) = \frac{K_0 g^2}{\omega^5}\exp\left[-\frac{5}{4}\left(\frac{\omega_0}{\omega}\right)^4\right]\gamma^r, \quad (19)$$

$$r = \exp\left[-\frac{(\omega-\omega_0)^2}{2\sigma^2\omega_0^2}\right], \quad (20)$$

Table 1
Input parameters for the modulated plane wave cases.

Case	f_0 [Hz]	a_0 [m]	$\Delta\omega$ [rad/s]	b_F	ψ	ϵ	Breaking?
MPW1	1.4	0.051	0.98	0.09	π	0.20	Yes
MPW2	1.5	0.031	1.05	0.06	π	0.14	No
MPW3	1.5	0.055	1.05	0.01	π	0.25	Yes
MPW4	1.6	0.039	1.60	0.05	π	0.20	Yes

Table 2
Input parameters for the focused wave groups and random waves based on the JONSWAP spectrum. Cases for which a focussing distance x_f is given correspond to focused wave groups, others to random waves.

Case	f_0 [Hz]	H_0 [m]	γ	x_f [m]	Breaking?
FGW1	0.91	0.01	3.30	18	No
FGW2	0.91	0.02	3.30	20	Yes
RDW1	1.11	0.02	3.30	–	No
RDW2	1.11	0.04	3.30	–	Rare
RDW3	1.11	0.06	3.30	–	Mild
RDW4	1.11	0.10	3.30	–	Extreme

$$\sigma = \begin{cases} 0.07 & \omega \le \omega_0, \\ 0.09 & \omega > \omega_0, \end{cases} \tag{21}$$

where K_0 is a scaling parameter to obtain appropriate wave height by the characteristic height H_0 and g (m/s^2) is the gravitational constant. For focused wave groups, phases are assigned by computing a linear phase shift from a given focussing distance x_f based on linear theory. For random waves, phases are randomised by a fixed random number seed and we follow the approach of Tucker et al. [28]. We recommend Eeltink et al. [19]'s article for further details. In Table 2 we list the focused wave group and the random wave cases that we investigate in Section 4.1.

The parameters for the randomly sampled focused wave group cases in Section 4.2 are drawn from the following ranges: $\gamma \in [2, 5]$, $H_0 \in [0.01, 0.06]$ m, $f_0 \in [0.5, 1.25]$ Hz, and $x_f \in [10, 24]$ m.

2.5. Numerical configuration

2.5.1. Numerical domain

We use two types of domains:

1. a non-periodic domain with wave inlet and zero-gradient outlet for comparison to experimental measurements in Section 4.1, the depth of the water is 0.8 m;
2. a periodic domain for focused wave group simulations with randomly sampled parameters in Section 4.2.

We keep all parameters the same between domains in order to maintain consistency between periodic and non-periodic simulations. The non-periodic simulation is for validation purposes only, and wherever a non-periodic domain is applied instead of its periodic counterpart, we will highlight this.

The periodic domain spans $[-26, 26]\lambda_0$ horizontally, where λ_0 is the length of the carrier wave or the spectral peak calculated by the linear dispersion relation $\omega_0^2 = k_0\, g\tanh(k_0 d)$. The depth of the water d is determined by $k_0 d = 5$, so that the water is considered to be deep. We use a square 2D domain, spanning $[-d, 52\lambda_0 - d]$ vertically. We only perform 2D simulations. By default, we restrict the Courant–Friedrichs–Lewy (CFL) number of the simulation to 0.1.

For the non-periodic domain, we use linear wave theory to determine the surface elevation η and the velocity vector $\mathbf{u}$ at the input boundary. We apply a Fourier Transform to decompose the measured surface elevation profile $\eta(t)$ at the first gauge in the experiment to obtain the amplitude and phase of the wave components. Then we compute the surface elevation and velocity vector using linear wave theory. We note that the error of linear wave theory increases rapidly when the input wave becomes steeper, and such a wave inlet boundary should be used with care. The non-periodic domain spans $52\lambda_0$ in the horizontal direction, and the wave inlet boundary aligns with the first gauge in the experiment.

We apply a zero-gradient condition for the top boundary and a no-slip condition for the bottom boundary. For the bottom boundary, we apply the Dirichlet condition for both κ and ω on a wall recommended in Menter [29]:

$$\kappa_{wall} = 0, \tag{22}$$

$$\omega_{wall} = 10\frac{6\mu}{\rho\beta_0(\Delta x)^2}. \tag{23}$$

To properly resolve ω near the bottom boundary, we enforce the resolution at the bottom boundary to the maximum (see Fig. 1).

The computational domain is always mapped via an affine transformation to the unit square $[0, 1] \times [0, 1]$ in $\mathcal{R}^2$. The refinement level L is defined as the number of subdivisions needed to reach the given cell starting from the unit square. By default, we set the grid refinement level in all simulations to $L = 14$, and we use three levels of refinement $L = 14, 15, 16$ to verify the convergence of the simulation. The corresponding grid width is calculated as $\Delta x = L_0/2^L$ where L_0 is the width of the computation domain. The impact of the maximum refinement level to the solution will be examined in Section 3. Through validation study, we find the minimum resolution required for our breaking wave study is $L = 14$. This will be a default setting in Section 4.

2.5.2. Characterising wave breaking

In order to perform simulations for which energy dissipation has converged (and numerical dissipation is thus negligible), the minimum length and time scales that need to be resolved must be determined in advance. Energy dissipation can be thought of as having two components: the effect of viscosity outside of wave breaking and dissipation during wave breaking. We aim at minimising viscous dissipation outside of wave breaking, because even in the laboratory-scale system, dissipation due to viscosity is insignificant as the Reynolds number of the system is of the order of 10^7. We do not model side-wall dissipation. To align with the experimental data, we will run the RANS simulations with Reynolds numbers as high as possible. In doing so, the aim is for viscous dissipation to be negligible outside of wave breaking, and dissipation due to breaking to dominate the energy evolution.

Wave-breaking dissipation is a highly non-linear process with different physical mechanisms coupled strongly with each other. To simplify the discussion, we follow Babanin [1] and split the process into two effects that contribute to the energy dissipation involved in breaking:

1. instant, transient (occuring within one wave period) breaking dissipation due to the mechanical failure of the breaking crest and bubble dynamics, and;
2. delayed, persistent dissipation (spans several wave periods) due to the turbulence formed during breaking.

To resolve the first effect, we choose the finest grid resolution near the wave surface to be close to the settings of the Mostert et al. [30]'s DNS simulation in order to resolve the evolution of the breaking crest, and we verify the convergence of our simulation by comparing the crest shape at breaking onset under different resolutions. To resolve the second effect, we use the RANS model to approximate the dissipation caused by the underwater turbulence formed during breaking.

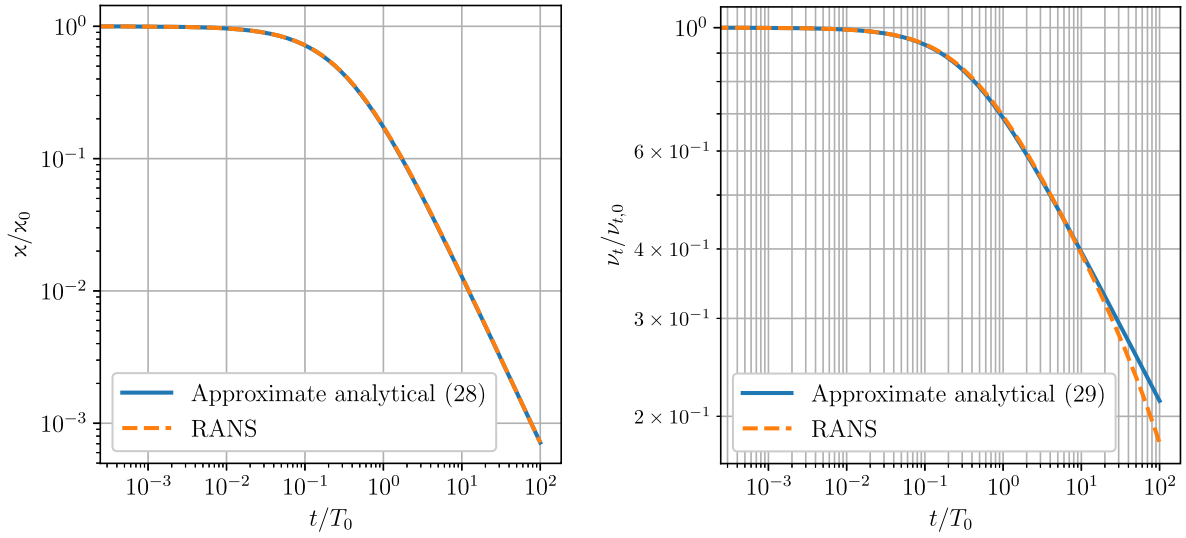

Fig. 2. Validation of the RANS turbulence model, showing the evolution of TKE and turbulent eddy viscosity of a Stokes wave and comparing the approximate analytical solution of decaying turbulence, Eqs. (28) and (29), in still water and RANS simulations.

The Reynolds number of the simulation is bounded by the maximum resolution that can be achieved with the available computational resources. Wave Reynolds number is defined as (e.g., Mostert et al. [30]):

$$\mathrm{Re} = \frac{\sqrt{g\lambda_0^3}}{\nu}, \tag{24}$$

where $g = 9.81\mathrm{m/s}^2$ is gravitational constant, λ_0 is carrier wavelength and ν is molecular viscosity. In previous studies, values of the wave Reynolds number of $\mathrm{Re} = 4\times10^4, 1\times10^5$ have been achieved in DNS simulations [30–32]. In this study, we run Stokes wave simulations with multiple Re numbers in Section 3 and we fix Re = 1,000,000 for all the simulations discussed in Section 4. We emphasise that such a range of Reynolds numbers is not reachable with fully resolved DNS at the present time.

We approximate the thickness of the viscous boundary layer to be $\delta = \sqrt{2\nu/\omega_0}$ where ω_0 is the angular velocity of the carrier wave [33].

The wave energy budget is made up of kinetic energy E_k and potential energy E_p. The energy budget together with its energy dissipation over time $E_d(t)$ due to molecular viscousity are obtained by integrating over the water phase (e.g., Mostert and Deike [34]):

$$E_k = \frac{1}{2}\int_\Omega \rho_w(\mathbf{u}\cdot\mathbf{u}/2)\mathrm{d}\Omega, \tag{25}$$

$$E_p = \int_\Omega \rho_w g h \mathrm{d}\Omega - E_{p,0}, \tag{26}$$

$$E_d(t) = \int_0^t\int_\Omega \mu\frac{\partial u_i}{\partial x_j}\frac{\partial u_j}{\partial x_i}\mathrm{d}\Omega\mathrm{d}t', \tag{27}$$

where Ω indicates the water domain, u, v are horizontal and vertical velocity, ρ_w is the water density, h is the height of a water element with respect to a reference level, and $E_{p,0}$ is the potential energy of still water with respect to the same level. The total energy budget $E_t = E_k + E_p + E_d$.

3. Validation of the RANS turbulence model

3.1. Non-breaking Stokes waves

To validate the model, we perform simulations of a non-breaking Stokes wave with different Reynolds numbers and examine energy conservation. We initialise the wave field with a third-order Stokes wave of amplitude a_0 and wavenumber k_0, setting the wave length $\lambda_0 = 2\pi/k_0 = 1.56$ m, the period $T_0 = 1$ s and steepness $\epsilon = a_0k_0 = 0.02$. The domain spans $[-\lambda_0, \lambda_0]$ in both horizontal and vertical directions. The simulation lasts $100T_0$. We set Re = 60,000, CFL = 0.12 and $\delta/\Delta x = 4$, where $\delta = \sqrt{2\nu/\omega_0}$.

In Fig. 2 we plot the integrated TKE and the turbulent eddy viscosity ν_t in the water phase and compare them to an approximate analytical solution for the decaying turbulence in still water. In still water, a reduced $\kappa-\omega$ model with only the unsteady, production and dissipation terms preserved leads to following analytical solution [35]:

$$\kappa = \kappa_0\left(1+\beta\omega_0 t\right)^{-\frac{\beta^*}{\beta}}, \tag{28}$$

$$\nu_t = \frac{\kappa_0}{\omega_0}\left(1+\beta\omega_0 t\right)^{1-\frac{\beta^*}{\beta}}, \tag{29}$$

where κ_0, ω_0 are the initial condition for κ and ω. For the standard $\kappa-\omega$ model, the TKE grows to become unbounded under the perturbation of potential-flow surface waves [14], but for the stabilised $\kappa-\omega$ model, no unbounded TKE growth is observed. The decaying TKE and ν_t match the analytical solution in Fig. 2.

In Fig. 3 we study the convergence of the wave energy budget by comparing different Reynolds numbers, maximum resolutions, and CFL numbers. In the top left panel we compare the energy budget for different Reynolds numbers. For Re = 60,000, 5% of the total energy is dissipated throughout the simulation. When an estimate of how much energy should have been dissipated is added back (top right panel), only 0.2% of the total energy is lost due to numerical dissipation, showing good convergence of the energy budget. For Re = 600,000, the energy dissipation shows a similar trend, but the amount of dissipation is much smaller. Adding an estimate of viscous dissipation leads to convergence at the level of 0.2%. For Re = 6,000,000, energy starts to increase slowly. The increase in energy remains as low as 0.4% over around 8 wave periods.

In the middle panels of Fig. 3, we compare the energy budget for different grid resolutions. The energy budget for $\delta/\Delta x = 4$ and 2 agrees well, but not for $\delta/\Delta x = 1$, demonstrating that the resolution of the viscous boundary layer should be at least $\delta/\Delta x = 2$ to achieve a converged energy budget.

In the bottom panels of Fig. 3, we investigate the influence of the CFL number. We note that the CFL number has a limited impact on the energy convergence at Re = 60,000. In the bottom right panel,

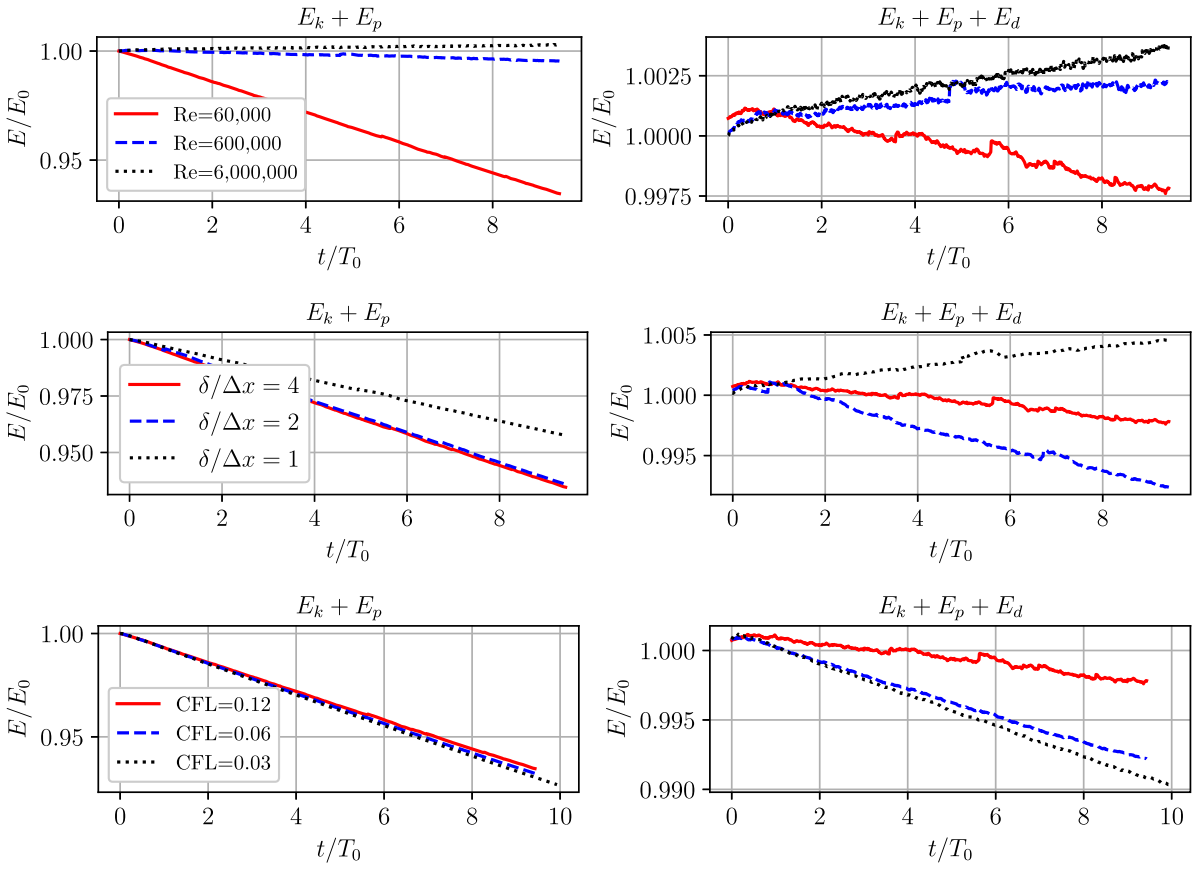

Fig. 3. Validation of the RANS turbulence model, showing the energy budget for a Stokes wave. Top panels compare the energy budget for three different Reynolds numbers, Re = 60,000, 600,000, 6,000,000. Middle panels display the energy budget for Re 60,000 with different grid resolutions, $\delta/\Delta x = 1, 2, 4$, where δ is the boundary layer thickness. Bottom panels plot the energy budget for Re 60,000 with CFL numbers CFL = 0.03, 0.06 and 0.12. In all panels, E_k, E_p and $E_d(t)$ are kinetic energy, potential energy and viscous dissipation integrated over the water phase and the time, respectively.

it becomes evident that the CFL number affects the amount of numerical dissipation. The smaller the CFL number, the more numerical dissipation introduced into the simulation.

In general, we find that energy conservation is achieved to an acceptable level throughout the simulation; the numerical error can be controlled to be below 1%. We can thus conclude that our implementation of a RANS model in Basilisk should be able to perform high-fidelity simulations for a reasonably large range of Reynolds numbers, given sufficient time and space resolution.

3.2. Breaking focused wave group

The space–time plot (Fig. 4) shows the details of the surface elevation evolution in a RANS simulation for case FGW2. The surface elevation profile $\eta(x,t)$ is shifted by its group speed. At $x \approx 19$ m, the wave group experiences focusing and wave breaking event within a short time. On the right side, three distinct panels (4b, 4c and 4d) correspond to the three selected spatial positions (pre-breaking, post-breaking and near-breaking positions) marked on the contour plot. Comparisons on the grid refinement levels $L = 14$, 15 and 16 indicate a good agreement between RANS simulations with different grid resolutions. By default, we use $L = 14$ for all simulations in Section 4.1.

4. Numerical results

In this section, we first reproduce the experiments of Eeltink et al. [19] listed in Table 2. We then compare the RANS simulation and experimental measurements to study the confidence level of our RANS method.

4.1. Comparison to the experiments of Eeltink et al. [19]

To compare with experimental measurements, we apply nonperiodic simulations with wave input from experimental measurements of the elevation profile of the surface on the first gauge ($x = 3.79$ m). Then we compare the surface elevation profiles measured at gauges located at position 3.79 m, 6.64 m, 8.82 m, 11.63 m, 13.73 m, 16.11 m, 18.78 m, 21.83 m, 24.53 m, 26.96 m, 29.10 m and 31.10 m, with the corresponding experimental measurements.

In Fig. 5, we compare the surface elevation profile of the RANS simulation with the gauge measurements of the experiment for the two focusing wave group cases listed in Table 2. The surface elevation profiles are shifted by its group speed. For case FGW1 (5a and 5b), there is no breaking event triggered. We find that the RANS simulation predicts surface elevation with satisfactory accuracy when compared to experimental measurements. The MSE is below 10^{-4}, suggesting a perfect match between experiment and RANS simulation.

For case FGW2 (5c and 5d), a breaking event occurs around $x = 18.78$ m, where the surface elevation becomes very steep. The prediction of the RANS simulation for this breaking event is in good agreement with the experimental observation. Although we only show 6 gauges near the breaking position in Fig. 5, in general we find that the RANS result agrees well with the experimental measurements at all gauges, and the RANS simulation is able to reproduce non-breaking wave evolution accurately. The MSE of case FGW2 starts from 10^{-6}, then grows rapidly during breaking, and ends up somewhere slightly above 10^{-4}. The 10^{-6} MSE level at the beginning indicates that our wave-inlet is able to reproduce the focused wave group input

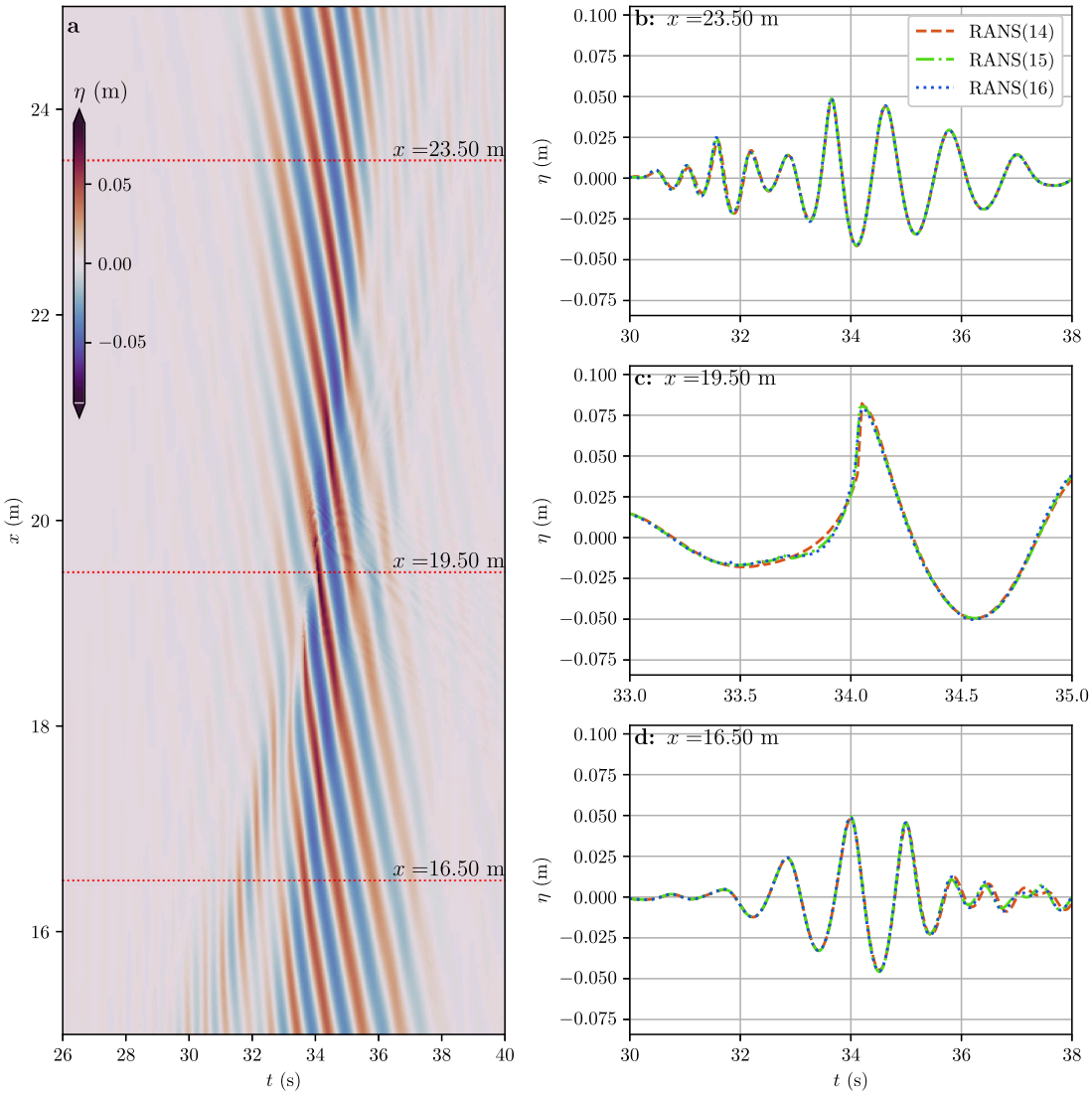

Fig. 4. This figure contains a space–time plot and wave height profiles at different locations for case FGW2 in Table 2. On the left (a), a space–time plot displays the evolution of surface elevation for RANS simulation with maximum refine level $L = 14$. The red dotted lines indicate the positions of the gauges. The right side contains three separate plots (b-d) at specific x locations (23.50 m, 19.50 m, 16.50 m), comparing the surface elevation over time as predicted by RANS simulations with different maximum refine level. The red dashed line is RANS simulation with maximum refine level $L = 14$, $L = 15$ for the green dot-dashed line and $L = 16$ for the blue dotted line. (For interpretation of the references to colour in this figure legend, the reader is referred to the web version of this article.)

accurately. The rapidly rising MSE level, however, suggesting that the breaking events have potentially significant impact to the accuracy of the RANS simulation. Despite that, 10^{-4} is still a very low MSE level and the post-breaking surface elevation profiles (such as the measurement at $x = 29.10$ m in Fig. 5) agrees well with the experimental measurements.

To investigate the performance of RANS simulation in more general scenarios, we further study the RANS simulation of modulated plane wave and random wave. In Fig. 6 we display the surface elevation profiles measured in 4 positions ($x = 3.79$ m, 8.82 m, 13.73 m, 18.78 m) for all 4 cases in Tables 1. The surface elevation profiles are shifted by its group speed. For all modulated plane wave cases, we note that the MSE starts from a relatively small value around $O(10^{-4})$, however, rapidly increases to 10^{-2}. This is mainly due to the mismatch of the wave breaking events. For case MPW1 (Fig. 6a), the breaking happens around $x = 13.73$ m, we find that the steepest crest in the surface elevation profile does not match to the experiment, indicating that the breaking happens in a different crest, or a different time in the simulation. Similar mismatches can be found in case MPW3 (Fig. 6e) and MPW4 (Fig. 6g) where the steepest crest does not match the experimental measurement. MSE of case MPW2 (Fig. 6d) increases slower because waves are shallow and no breaking is triggered. We present variance, skewness and kurtosis of the surface elevation profile at the wave-input boundary and compare them to experiments in Appendix. For modulated plane wave cases, the statistics of the wave agree well to the experiment at the wave-input boundary, suggesting that the wave profile is reproduced reliably. The mismatch may be caused by an unknown error in the experiment or by chaotic behaviour during the previous breaking procedure [36].

In Fig. 7 we display the surface elevation profiles measured in 4 positions (same as the modulated plane wave cases) for all random wave cases listed in Table 2. For random wave cases, the MSE scales up quickly with the characteristic wave height H_0 (also the significant wave height for random wave cases). We also find that the MSE starts from $O(10^{-2})$, indicating that the wave input error is large. For case RDW4 (Fig. 7g), the simulation deviates a lot from the experimental measurement in the last 2 gauges. We believe this is due to the fact that case RDW4 has an exceedingly high H_0, resulting in frequent and

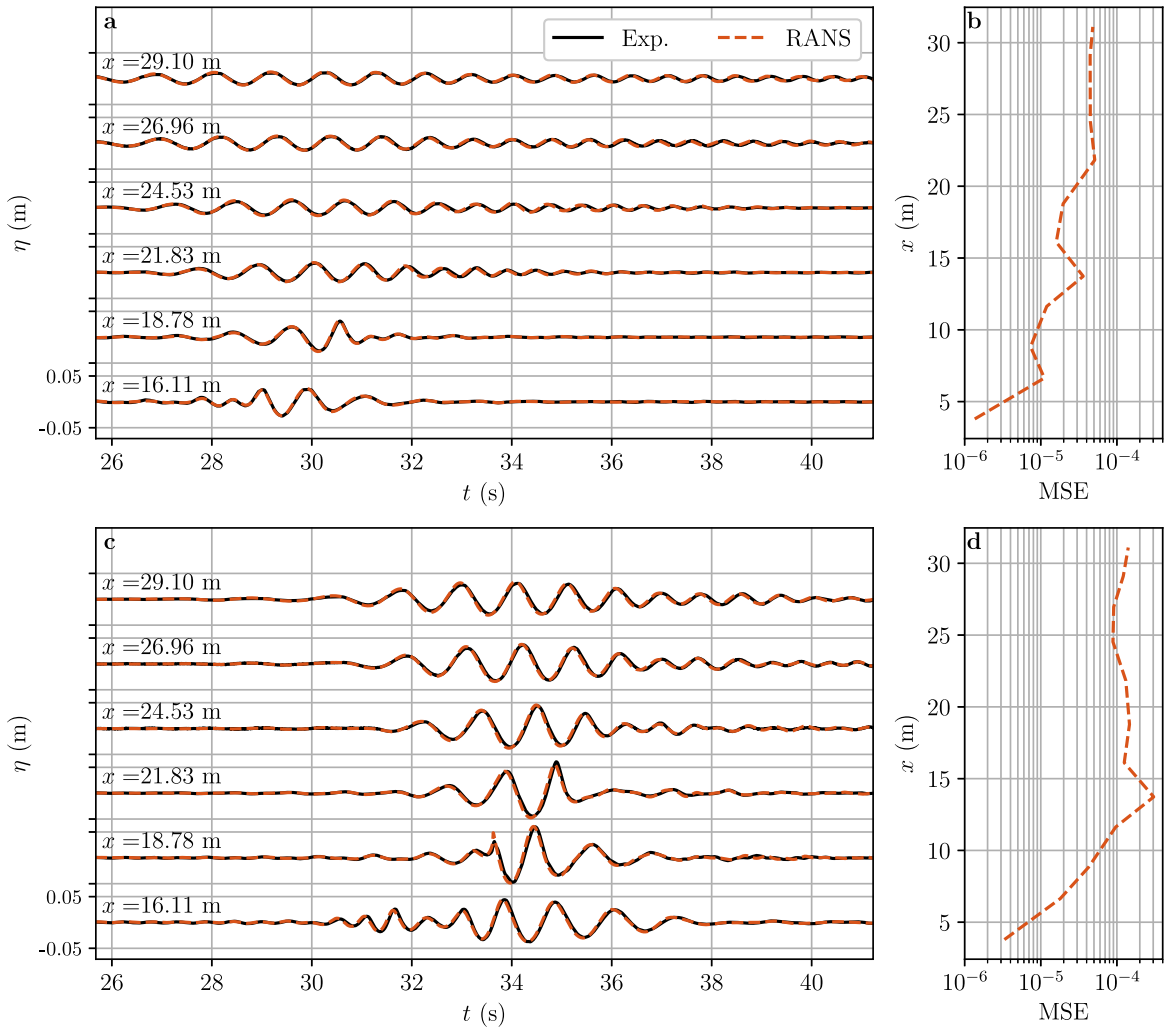

Fig. 5. This figure plots the surface elevation profiles at multiple gauge positions for all focused wave cases in Table 2 and compares the experimental measurements and RANS simulation at different gauge positions. The top panels (a and b) are for case FGW1 and the bottom panels (c and d) are for case FGW2.

intense breaking that deteriorates the quality of the simulation quickly. A detailed discussion on the variance, skewness and kurtosis of the surface elevation profile at the wave-input boundary is in Appendix. For random wave cases, the variance does not align well with experimental measurements and the error scales with the steepness. This is due to the failure of the linear assumption of the input wave. The mismatch of the breaking event may be caused by multiple factors that have been discussed so far.

4.2. Random periodic domain simulations

Our aim is to perform high Reynolds number energy-resolving RANS simulations in a periodic domain for purpose of generating high quality training data for physics-based neural networks. We have built trust in our numerical setup by examining the Stokes wave simulation. We have shown that the simulation is in agreement with the experiment for cases with a few breaking events by studying the non-periodic wave simulations and comparing them to experimental data. In this section, we apply RANS to study focused wave breaking in the periodic domain.

In Fig. 8 we plot 4 snapshots of the flow field in one of the periodic simulations of focused wave group cases, showing the evolution of the water-air interface and the turbulent eddy viscosity in the water domain. We find that coherent structures such as overturning crests, jet splashing, and bubble formation during breaking are resolved successfully. Turbulent cores with high turbulent eddy viscosity ($\geq 100\nu_w$) are produced during breaking events. The turbulent cores span around 1 carrier wavelength and have negligible drifting after settling down.

Fig. 9 shows the evolution of the kinetic energy, the potential energy and the total energy of the simulation. We find that the total energy is well conserved in the nonbreaking interval. The total energy loss during the entire duration is around 2%. The potential energy oscillates slightly because there are subgrid-scale waves brought by the initial condition of surface elevation that interfere with each other.

Fig. 10 displays the nondimensional energy dissipation parameter b as a result of breaking when plotted against ϵ, where in focused wave cases we define $\epsilon = \sum_i a_i k_i$ as the max linear slope. We plot randomly generated FGW cases with $\epsilon \in [0.28, 0.38]$ and other parameter ranges provided in Section 2.4.2. b is calculated with Drazen et al. [20]'s approach:

$$b = \frac{g^2 c_g \int_{t_1}^{t_2} (\eta_1^2 - \eta_2^2) dt}{T_b c_b^5}, \tag{30}$$

where g is gravitational constant, $c_g = \omega_0/2k_0$ is the carrier group speed, η_1 and η_2 is the surface elevation profile at far upstream and downstream of the breaking event where we assume the wave is not so steep and the equipartition of energy is valid. The control volume

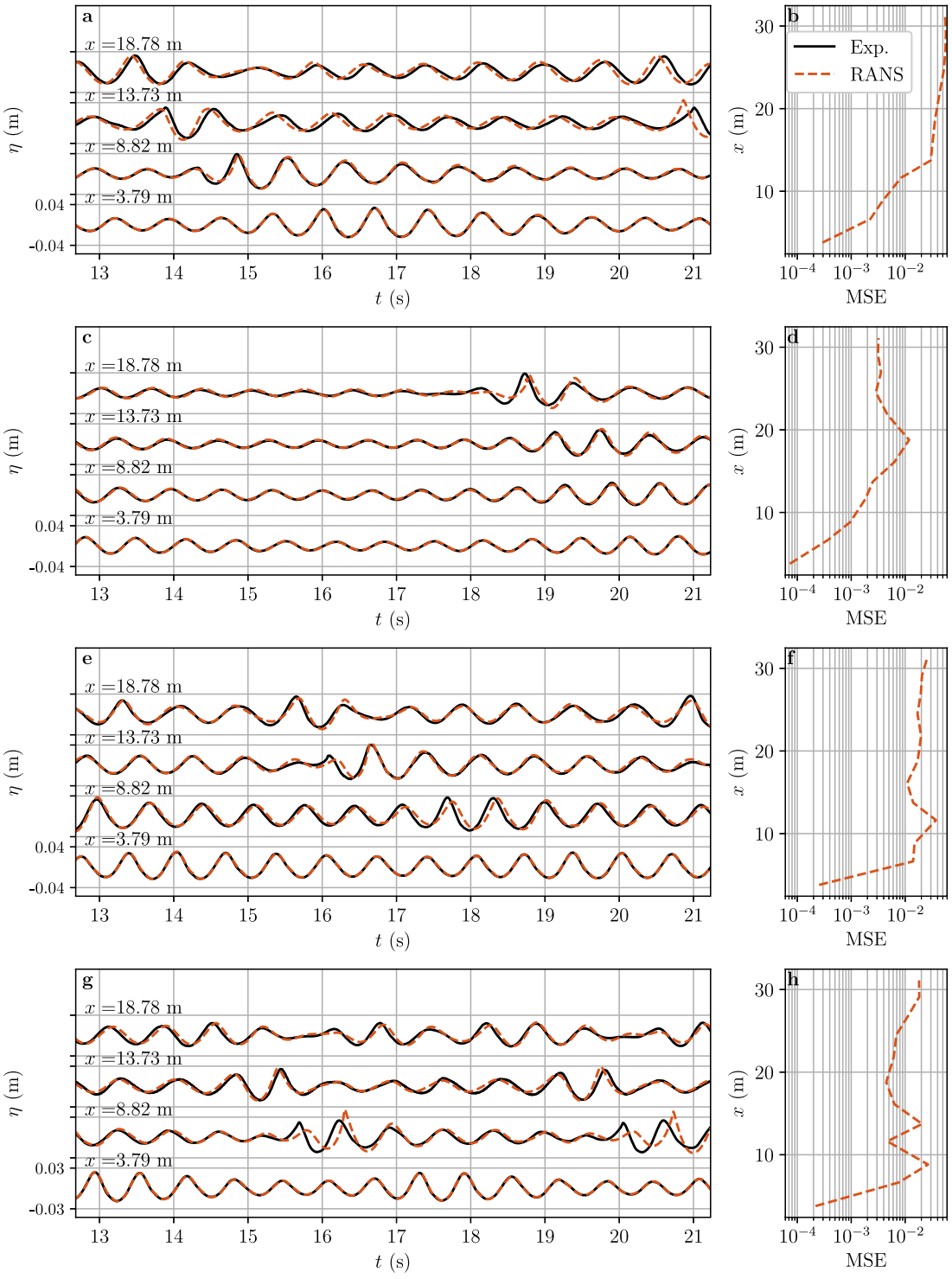

Fig. 6. This figure plots the surface elevation profiles at multiple gauge positions for all modulated plane wave cases in Table 1 and compares the experimental measurements and RANS simulation at different gauge positions. Panels (a) and (b): case MPW1; Panels (c) and (d): case MPW2; Panels (e) and (f): case MPW3; Panels (g) and (h): case MPW4.

in time $t \in [t_1, t_2]$ wraps the wave group so that $\int_{t_1}^{t_2}(\eta_1^2 - \eta_2^2)dt \approx \int_{-\infty}^{+\infty}(\eta_1^2 - \eta_2^2)dt$. The breaking onset is defined as when the local slope η_x exceeds 0.5774 [1,37], and the active breaking interval T_b is estimated to be $0.5T_0$ [38]. The breaking crest speed c_b is estimated to be 80% of the speed of the carrier phase speed ω_0/k_0 [39].

We find that all the present RANS data fall within the range of ±1 standard deviation, giving confidence to the energy dissipation resolved in the RANS simulations. We note that in most cases the measured breaking parameter b is slightly lower than the empirical curve, but the deviation is lower than the uncertainties reported in the previous study of Mostert et al. [30].

5. Conclusions

This paper utilised RANS simulation with Basilisk to study the deep water wave breaking problem. We validated the numerical configurations with Stokes wave simulation. We then used the RANS model to simulate wave breaking in focused wave groups, modulated plane

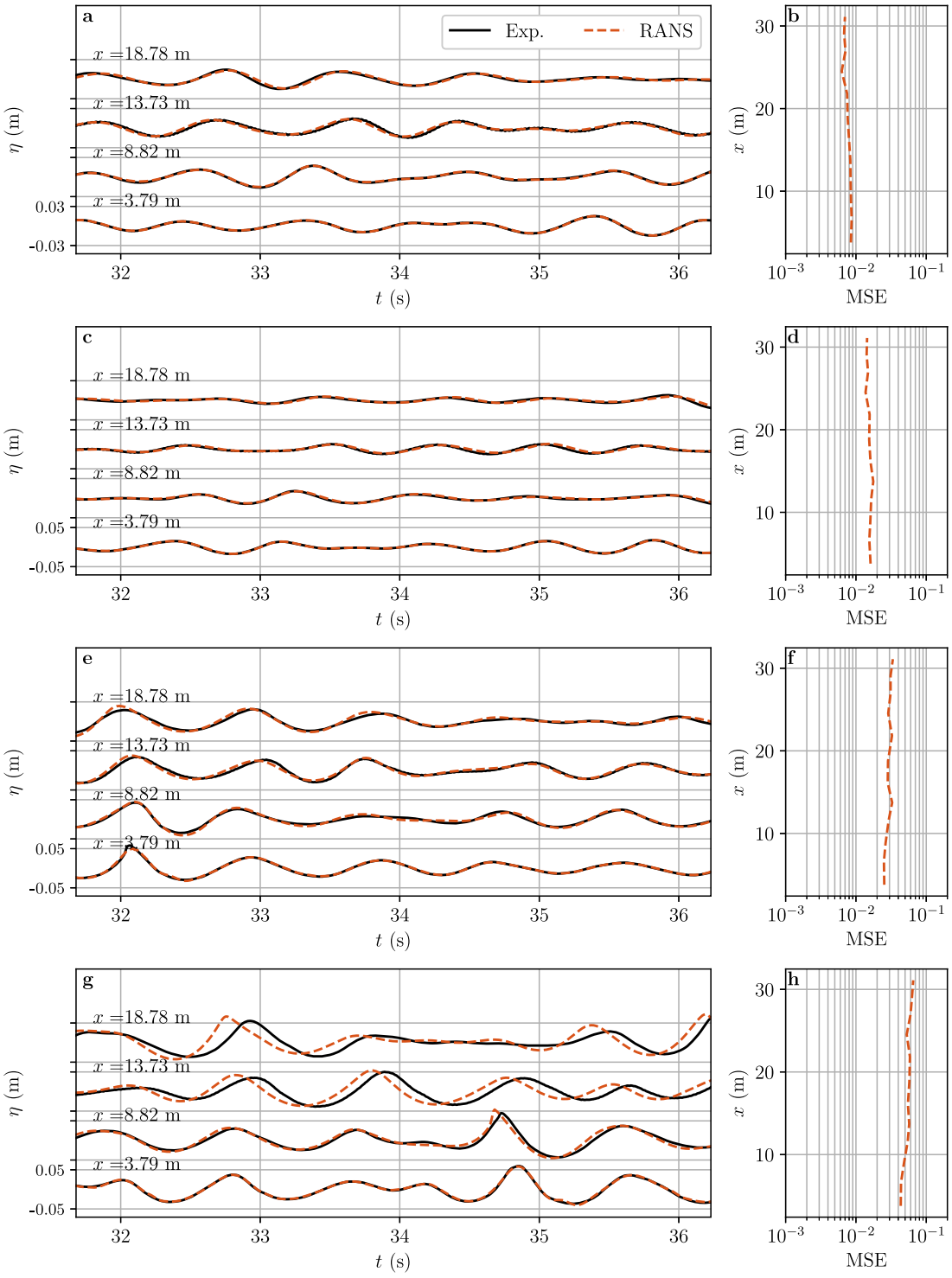

Fig. 7. This figure plots the surface elevation profiles at multiple gauge positions for all random wave cases in Table 2 and compares the experimental measurements and RANS simulation at different gauge positions. Panels (a) and (b): case RDW1; Panels (c) and (d): case RDW2; Panels (e) and (f): case RDW3; Panels (g) and (h): case RDW4.

waves, and random waves with JONSWAP spectrum. The RANS simulation was found to be in agreement with the gauge measurements from the experiment. Additionally, we applied the RANS simulation to perform a large number of focused wave group simulations in the periodic domain. We discovered that the energy was nearly conserved in the nonbreaking region. We also studied the breaking parameter b, showing that the breaking parameter in our simulation agrees well with previous studies.

By verifying the RANS model, we can take advantage of the limitation of the Reynolds number. Compared to the traditional DNS approach used in Basilisk, which is limited to a Reynolds number of $O(10^4)$, RANS simulations can be conducted in a much broader range, from 10^4 to 10^7. This enables us to simulate a system on a laboratory scale with reasonable computational resources.

During the preparation of this work the authors used ChatGPT and Overleaf AI text service in order to improve readability. After using this

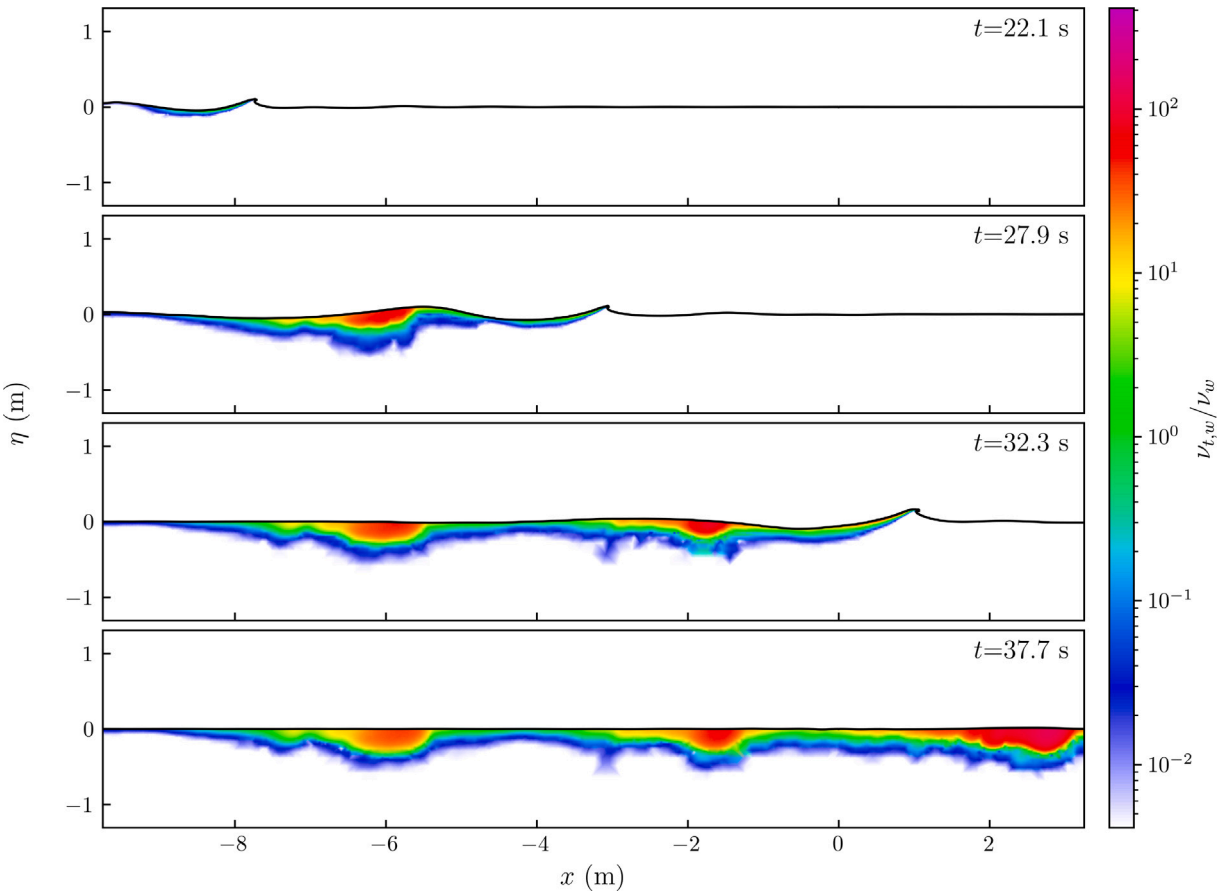

Fig. 8. The evolution of interface and turbulent visocity $\nu_{t,w}$ in water domain.

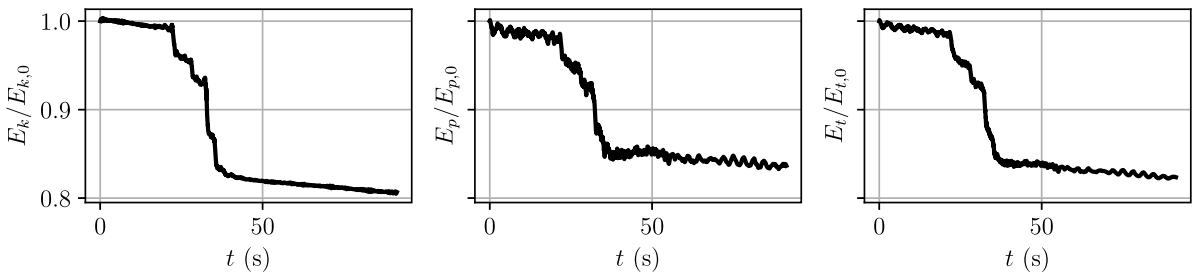

Fig. 9. This figure plots the evolution of kinetic energy E_k, potential energy E_p and total energy E_t of the periodic simulation of a focused group wave case.

tool, the authors reviewed and edited the content as needed and take full responsibility for the content of the publication.

CRediT authorship contribution statement

Yuxuan Liu: Writing – original draft, Visualization, Software, Methodology, Investigation, Formal analysis, Conceptualization. **Ton S. van den Bremer:** Writing – review & editing, Supervision. **Thomas A.A. Adcock:** Writing – review & editing, Supervision.

Declaration of competing interest

The authors declare that they have no known competing financial interests or personal relationships that could have appeared to influence the work reported in this paper.

Data availability

Data will be made available on request.

Appendix. Statistics of the non-periodic cases

We present the variance, skewness and kurtosis of all the non-periodic cases investigated in this study. We analyse the surface elevation profiles measured at gauges located at position 3.79 m, 6.64 m, 8.82 m, 11.63 m, 13.73 m, 16.11 m, 18.78 m, 21.83 m, 24.53 m, 26.96 m, 29.10 m and 31.10 m, with the corresponding experimental measurements. The part $f > 5.0f_0$ and the part $f < 0.1f_0$ of the profile frequency spectrum are filtered, where f_0 is the carrier frequency. We then normalise the surface elevation profiles by dividing the standard deviation of the first gauge of the experimental measurement. The formulas to calculate variance, skewness and kurtosis are written as follows:

$$\text{Variance}(\eta) = \frac{1}{N}\sum_{i=1}^{N}(\eta_i - \bar{\eta})^2, \tag{31}$$

$$\text{Skewness}(\eta) = \frac{\frac{1}{N}\sum_{i=1}^{N}(\eta_i - \bar{\eta})^3}{\left(\frac{1}{N}\sum_{i=1}^{N}(\eta_i - \bar{\eta})^2\right)^{3/2}}, \tag{32}$$

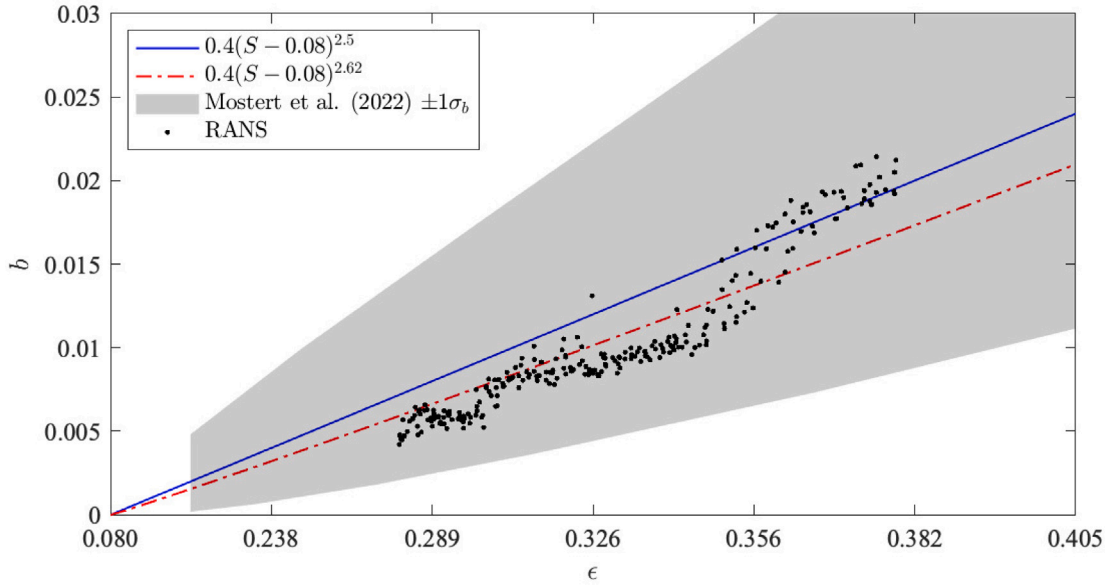

Fig. 10. This figure plots breaking parameter b against the max linear slope ϵ. Blue solid line is a semi-empirical formula [21]. Red dot-dashed line is an exponential fit $b = 0.4(\epsilon - 0.08)^q$ to the RANS data where $q = 2.62$. Grey shaded region is standard deviation $\pm 1\sigma_b$ on the scaling for b. Black dots indicates calculated parameter b of RANS data. (For interpretation of the references to colour in this figure legend, the reader is referred to the web version of this article.)

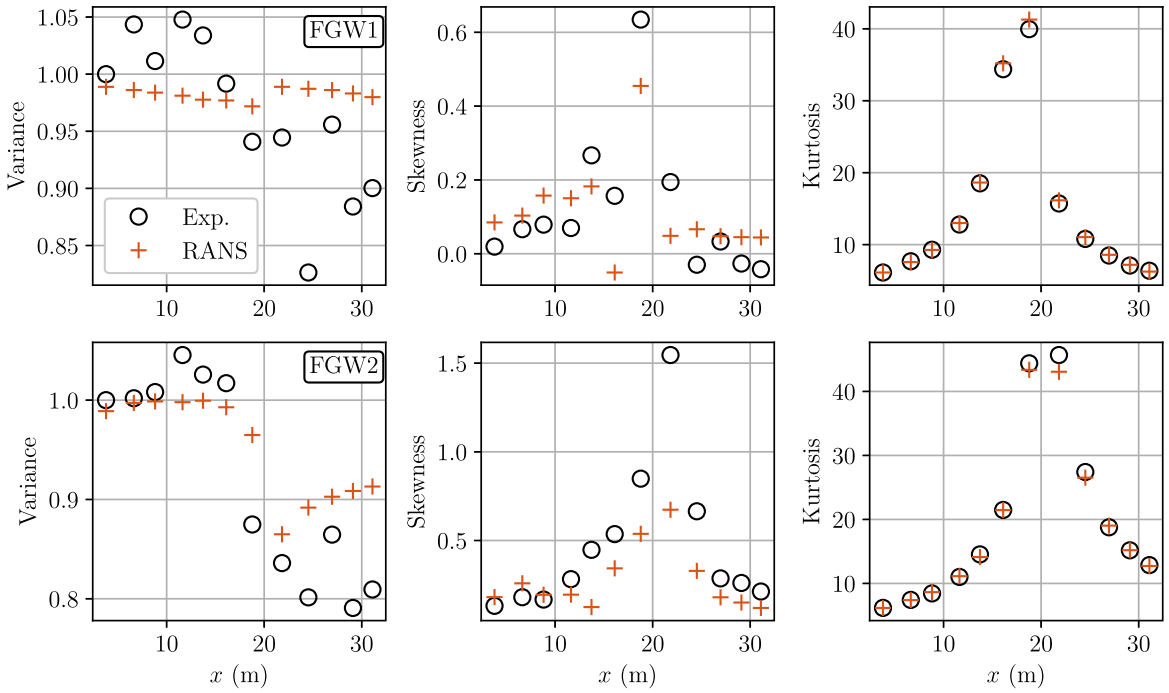

Fig. 11. This figure plots the variance, skewness and kurtosis of the normalised surface elevation profiles at multiple gauge positions for all focused wave cases in Table 2 and compares the experimental measurements and RANS simulation at different gauge positions.

$$\text{Kurtosis}(\eta) = \frac{\frac{1}{N}\sum_{i=1}^{N}(\eta_i - \bar{\eta})^4}{\left(\frac{1}{N}\sum_{i=1}^{N}(\eta_i - \bar{\eta})^2\right)^2}. \tag{33}$$

In Fig. 11 we plot the variance, skewness, and kurtosis of the focused wave cases in Table 2. We found that the statistics of the first gauge (at the wave-inlet boundary) agree well with the experiment. The fluctuation of the variance and skewness is around 10% for case FGW1. The RANS variance of case FGW2 increases, while the experimental measurement shows a decreasing trend. The skewness of case FGW2 is severely underestimated when compared to the experiment. Kurtosis is excessively high, indicating that the focused wave cases do not comply with the normal distribution. The kurtosis of the RANS simulation agrees well with the experiment for both FGW1 and FGW2.

In Fig. 12 we plot the statistics of the modulated plane wave cases in Table 1. We found that the statistics of the first gauge match well with the experiment, indicating that the wave profile is reproduced successfully at the wave-input boundary.

In Fig. 13 we plot the statistics of the random wave cases in Table 2. We found that the variance of the first gauge is underestimated for more than 10% compared to the experiment. The difference in variance

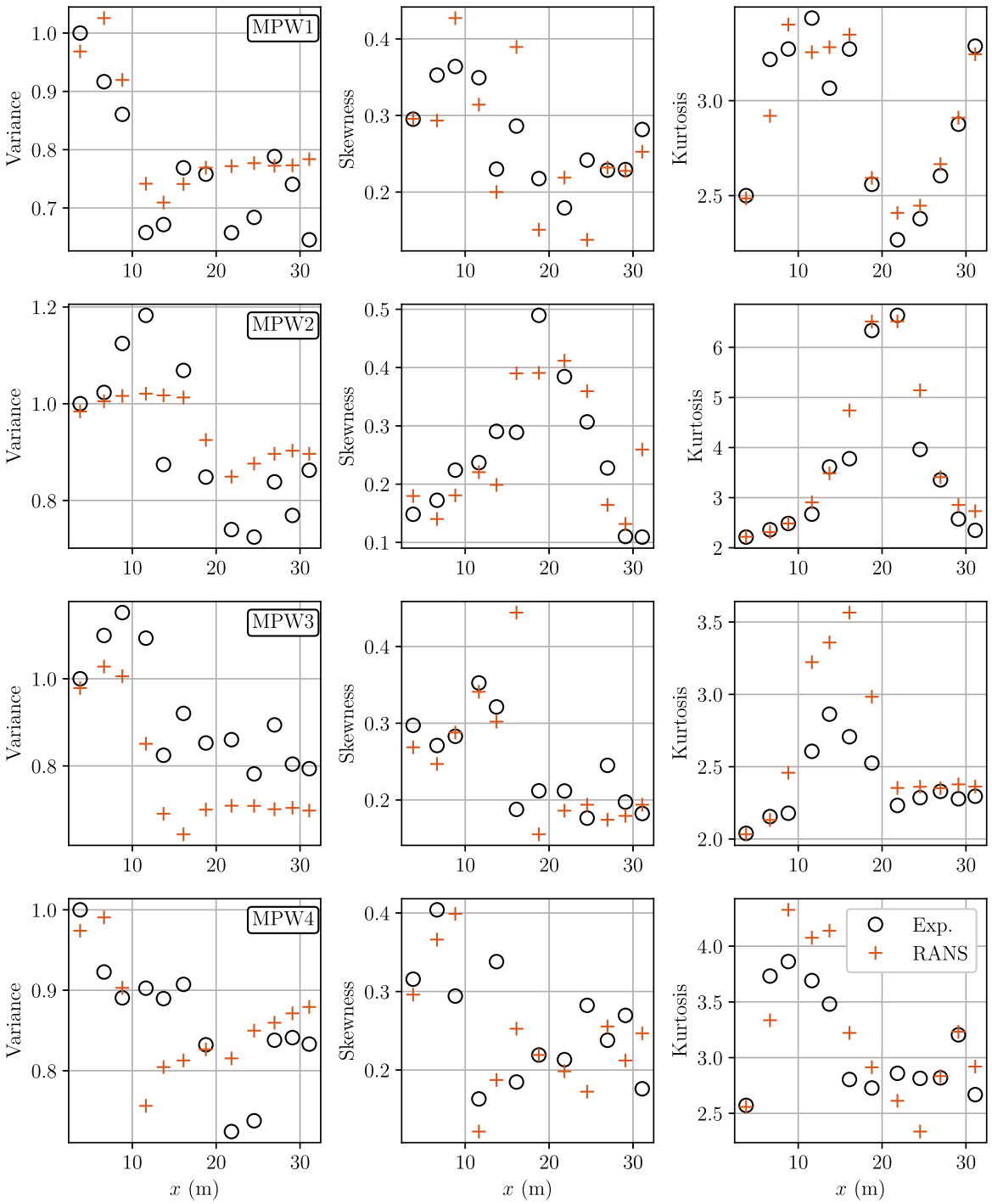

Fig. 12. This figure plots the variance, skewness and kurtosis of the normalised surface elevation profiles at multiple gauge positions for all modulated plane wave cases in Table 1 and compares the experimental measurements and RANS simulation at different gauge positions.

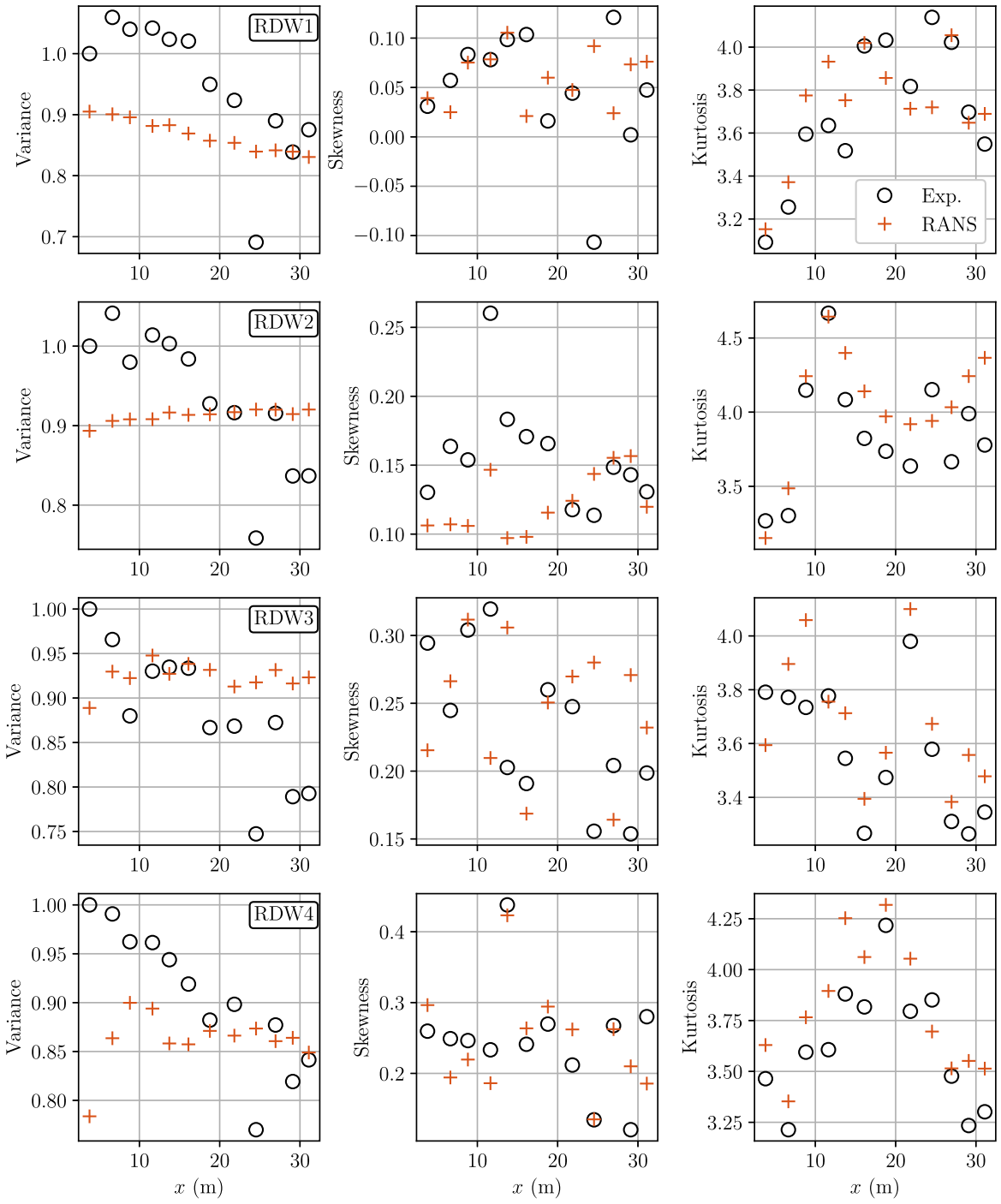

Fig. 13. This figure plots the variance, skewness and kurtosis of the normalised surface elevation profiles at multiple gauge positions for all random wave cases in Table 2 and compares the experimental measurements and RANS simulation at different gauge positions.

exceeds 20% for steeper case, i.e., RDW4, indicating that our wave-input boundary cannot produce very steep waves. The skewness does not align well with the experimental data. We cannot identify any patterns from the error, nor we can detect any consistent trend towards either overestimation or underestimation. The kurtosis of the RANS simulation exhibits slight overestimation and generally follows the results of the experiment.

References

[1] A. Babanin, Breaking and Dissipation of Ocean Surface Waves, Cambridge University Press, 2011.
[2] P. Lin, P.L.-F. Liu, A numerical study of breaking waves in the surf zone, J. Fluid Mech. 359 (1998) 239–264, Publisher: Cambridge University Press.
[3] S.F. Bradford, Numerical simulation of surf zone dynamics, J. Waterw. Port Coast. Ocean Eng. 126 (1) (2000) 1–13, Publisher: American Society of Civil Engineers (ASCE).
[4] Z. Xie, Two-phase flow modelling of spilling and plunging breaking waves, Appl. Math. Model. 37 (6) (2013) 3698–3713.
[5] J.-S. Zhang, Y. Zhang, D.-S. Jeng, P.L.-F. Liu, C. Zhang, Numerical simulation of wave–current interaction using a RANS solver, Ocean Eng. 75 (2014) 157–164.
[6] I. López, B. Pereiras, F. Castro, G. Iglesias, Optimisation of turbine-induced damping for an OWC wave energy converter using a RANS–VOF numerical model, Appl. Energy 127 (2014) 105–114, Publisher: Elsevier Ltd.

[7] M. Colombo, M. Fairweather, Multiphase turbulence in bubbly flows: RANS simulations, Int. J. Multiph. Flow 77 (2015) 222–243, Publisher: Elsevier Ltd.
[8] B. Devolder, P. Troch, P. Rauwoens, Performance of a buoyancy-modified k-ω and k-ω SST turbulence model for simulating wave breaking under regular waves using OpenFOAM®, Coast. Eng. 138 (2018) 49–65, Publisher: Elsevier B.V.
[9] B.E. Larsen, D.R. Fuhrman, On the over-production of turbulence beneath surface waves in Reynolds-averaged Navier–Stokes models, J. Fluid Mech. 853 (2018) 419–460, Publisher: Cambridge University Press.
[10] Y. Li, B.E. Larsen, D.R. Fuhrman, Reynolds stress turbulence modelling of surf zone breaking waves, J. Fluid Mech. 937 (2022) A7.
[11] S. Mayer, P.A. Madsen, Simulation of breaking waves in the surf zone using a Navier-Stokes solver, in: Coastal Engineering 2000, American Society of Civil Engineers, 2001, pp. 928–941.
[12] D. Wilcox, Turbulence Modeling for CFD, third ed., DCW Industries, 2006.
[13] D.C. Wilcox, Formulation of the k-w turbulence model revisited, AIAA J. 46 (11) (2008) 2823–2838.
[14] B.E. Larsen, D.A.v.d. A, J.v.d. Zanden, G. Ruessink, D.R. Fuhrman, Stabilized RANS simulation of surf zone kinematics and boundary layer processes beneath large-scale plunging waves over a breaker bar, Ocean Model. 155 (2020) 101705.
[15] D.R. Fuhrman, Y. Li, Instability of the realizable k–ϵ turbulence model beneath surface waves, Phys. Fluids 32 (11) (2020) 115108.
[16] V. Gruwez, C. Altomare, T. Suzuki, M. Streicher, L. Cappietti, A. Kortenhaus, P. Troch, Validation of RANS modelling for wave interactions with sea dikes on shallow foreshores using a large-scale experimental dataset, J. Mar. Sci. Eng. 8 (9) (2020) 650.
[17] N. Ahmad, H. Bihs, D. Myrhaug, A. Kamath, Ø.A. Arntsen, Numerical modelling of pipeline scour under the combined action of waves and current with free-surface capturing, Coast. Eng. 148 (2019) 19–35.
[18] Y. Li, D.R. Fuhrman, CFD simulation of nonlinear deep-water wave instabilities involving wave breaking, in: Volume 6: Ocean Engineering, American Society of Mechanical Engineers, 2021.
[19] D. Eeltink, H. Branger, C. Luneau, Y. He, A. Chabchoub, J. Kasparian, T.S. Van Den Bremer, T.P. Sapsis, Nonlinear wave evolution with data-driven breaking, Nature Commun. 13 (1) (2022) 2343.
[20] D.A. Drazen, W.K. Melville, L. Lenain, Inertial scaling of dissipation in unsteady breaking waves, J. Fluid Mech. 611 (2008) 307–332, Publisher: Cambridge University Press.
[21] L. Romero, W.K. Melville, J.M. Kleiss, Spectral energy dissipation due to surface wave breaking, J. Phys. Oceanogr. 42 (9) (2012) 1421–1444.
[22] S. Popinet, An accurate adaptive solver for surface-tension-driven interfacial flows, J. Comput. Phys. 228 (16) (2009) 5838–5866.
[23] F.G. Schmitt, About Boussinesq's turbulent viscosity hypothesis: historical remarks and a direct evaluation of its validity, C. R. Mécanique 335 (9–10) (2007) 617–627.
[24] C. Rumsey, Notes on running the cases with CFD, 2023, Turbulence modeling resource. https://turbmodels.larc.nasa.gov/noteonrunning.html.
[25] S.B. Pope, An explanation of the turbulent round-jet/plane-jet anomaly, AIAA J. 16 (3) (1978) 279–281.
[26] N. Oumrani, M. Aouissi, A. Bounif, B. Yssaad, F. Tabet, I. Gokalp, A first- and second-order turbulence models in hydrogen non-premixed flame, Int. J. Heat Technol. 33 (3) (2015) 27–34.
[27] K. Hasselmann, T. Barnett, E. Bouws, H. Carlson, D. Cartwright, K. Enke, J. Ewing, H. Gienapp, D. Hasselmann, P. Kruseman, A. Meerburg, P. Muller, D. Olbers, K. Richter, W. Sell, H. Walden, Measurements of wind-wave growth and swell decay during the Joint North Sea Wave Project (JONSWAP), Deut. Hydrogr. Z. 8 (1973) 1–95.
[28] M. Tucker, P. Challenor, D. Carter, Numerical simulation of a random sea: a common error and its effect upon wave group statistics, Appl. Ocean Res. 6 (2) (1984) 118–122.
[29] F. Menter, Zonal two equation k-w turbulence models for aerodynamic flows, in: 23rd Fluid Dynamics, Plasmadynamics, and Lasers Conference, American Institute of Aeronautics and Astronautics, Orlando, FL, U.S.A., 1993.
[30] W. Mostert, S. Popinet, L. Deike, High-resolution direct simulation of deep water breaking waves: transition to turbulence, bubbles and droplets production, J. Fluid Mech. 942 (2022) A27, Publisher: Cambridge University Press.
[31] A. Iafrati, Numerical study of the effects of the breaking intensity on wave breaking flows, J. Fluid Mech. 622 (2009) 371–411, Publisher: Cambridge University Press.
[32] L. Deike, N. Pizzo, W.K. Melville, Lagrangian transport by breaking surface waves, J. Fluid Mech. 829 (2017) 364–391, Publisher: Cambridge University Press.
[33] M.S. Longuet-Higgins, Mass transport in water waves, Philos. Trans. R. Soc. Lond. Ser. A Math. Phys. Sci. 245 (903) (1953) 535–581.
[34] W. Mostert, L. Deike, Inertial energy dissipation in shallow-water breaking waves, J. Fluid Mech. 890 (2020) A12, Publisher: Cambridge University Press.
[35] S.B. Pope, Turbulent Flows, Cambridge University Press, 2000.
[36] Z. Wei, C. Li, R.A. Dalrymple, M. Derakhti, J. Katz, Chaos in breaking waves, Coast. Eng. 140 (2018) 272–291.
[37] M.L. McAllister, N. Pizzo, S. Draycott, T.S. Van Den Bremer, The influence of spectral bandwidth and shape on deep-water wave breaking onset, J. Fluid Mech. 974 (2023) A14, arXiv:2305.08614 [physics].
[38] M. Derakhti, M.L. Banner, J.T. Kirby, Predicting the breaking strength of gravity water waves in deep and intermediate depth, J. Fluid Mech. 848 (2018) R2, Publisher: Cambridge University Press.
[39] X. Barthelemy, M.L. Banner, W.L. Peirson, F. Fedele, M. Allis, F. Dias, On a unified breaking onset threshold for gravity waves in deep and intermediate depth water, J. Fluid Mech. 841 (2018) 463–488, Publisher: Cambridge University Press (CUP).